Available online at www.sciencedirect.com

jmr&t
Journal of Materials Research and Technology

journal homepage: www.elsevier.com/locate/jmrt

Corrosion resistance and microstructure analysis of additively manufactured 22% chromium duplex stainless steel by laser metal deposition with wire

Amir Baghdadchi [a,*], *Claire Cary* [b], *Narasi Sridhar* [b],
Maria Asuncion Valiente Bermejo [a], *Carolin Fink* [b], *Joel Andersson* [a]

[a] *Department of Engineering Science, University West, 461 86 Trollhättan, Sweden*
[b] *Department of Materials Science and Engineering, The Ohio State University, Columbus, OH 43221, USA*

ARTICLE INFO

Article history:
Received 7 July 2023
Accepted 5 September 2023
Available online 9 September 2023

Keywords:
Additive manufacturing
Duplex stainless steel
Laser metal deposition
Localized corrosion
Microstructure-property relation

ABSTRACT

Microstructure characteristics and pitting corrosion of a duplex stainless steel (DSS) manufactured by laser metal deposition with wire (LMDw) were studied. The layer-by-layer LMDw process resulted in a mixed microstructure of predominantly ferrite with 2% austenite and chromium-rich nitrides, and reheated regions with ~33% austenite. The high cooling rate of LMDw restricted the distribution of Cr, Mo, and Ni, in ferrite and austenite, while N diffuses from ferrite to austenite. Subsequent heat treatment at 1100 °C for 1 h resulted in homogenized microstructure, dissolution of nitrides, and balanced ferrite/austenite ratio. It also led to the redistribution of Cr and Mo to ferrite, and Ni and N to austenite. At room temperature, cyclic potentiodynamic polarization measurements in 1.0 M NaCl solution showed no significant differences in corrosion resistance between the as-deposited and heat-treated samples, despite the differences in terms of ferrite to austenite ratio and elemental distribution. Critical pitting temperature (CPT) was the lowest (60 °C) for the predominantly ferritic microstructure with finely dispersed chromium-rich nitrides; while reheated area with ~33% austenite in as-deposited condition achieved higher critical temperature comparable to what was obtained after heat treatment (73 and 68 °C, respectively). At temperatures above the CPT, selective dissolution of the ferrite after deposition was observed due to depletion of N, while after heat treatment, austenite preferentially dissolved due to Cr and Mo concentrating in ferrite. In summary, results demonstrate how microstructural differences in terms of ferrite-to-austenite ratio, distribution of corrosion-resistant elements, and presence of nitrides affect corrosion resistance of LMDw DSS.

1. Introduction

Additive manufacturing (AM) has provided new opportunities to fabricate near-net-shape duplex stainless steel (DSS) components with reduced material waste, tailored properties, and high design complexity [1]. Over the years, remarkable advancements in AM have led to its adoption in various industry sectors for producing complex 3D geometries in a single step. Furthermore, AM has introduced appealing

---

* Corresponding author.
E-mail address: amir.baghdadchi@hv.se (A. Baghdadchi).

https://doi.org/10.1016/j.jmrt.2023.09.037

properties and posed fresh challenges in part fabrication, which were previously unattainable through conventional manufacturing methods. For metallic materials, powder bed fusion (PBF) and direct energy deposition (DED) are 2 a.m. technologies that are primarily used for part fabrication. Laser metal deposition with wire (LMDw) as a DED technique employs a laser beam energy source to melt wire and deposit the material in a layer-by-layer fashion to build the component [2]. The process uses low cost feedstock (wire) and is highly material efficient (up to 100%). In addition, LMDw typically has a high productivity as compared to powder-based AM techniques [3]. The implementation of hot-wire technology further enhances the deposition rate of LMDw, leading to improved productivity [4,5].

Duplex stainless steels (DSS) receive much attention for different industrial applications such as pressure vessels, heat exchangers, and underwater infrastructure. This is due to a high corrosion resistance along with excellent mechanical properties. These materials exhibit a mixed ferrite-austenite structure. Optimum properties are obtained by a balance of ferrite and austenite phases, which can be altered by composition and thermal processing. The amount of alloying elements (in particular Cr, Mo and N) and microstructure determine to a large extend the general corrosion resistance and the resistance to localized corrosion (pitting and crevice) [6]. Highly alloyed DSS grades show an improved corrosion resistance. The pitting corrosion resistance of DSS has been correlated to the pitting resistance equivalent number (PREN $=$ % Cr $+$ 3.3% Mo $+$ 16% N) [7], although such correlations have to be used with care for different environments [8] and microstructural conditions. Corrosion resistance is typically reduced by the presence of intermetallics and nitrides. Local regions of Cr and Mo depletion result in sensitization, and increases susceptibility to pitting and crevice corrosion [9–14].

Due to the high cooling rates typical for high energy density processes such as laser welding and laser additive manufacturing, it can be challenging to achieve a proper phase and composition balance when fabricating DSS because of the high amount of ferrite and large number of nitrides that form [15,16]. In AM, layer-by-layer deposition results in secondary austenite to form in reheated regions of the build microstructure. This can lead to a degradation in mechanical properties and corrosion resistance [17,18]. This is because of the lower concentration of Cr, Mo, and N in the secondary austenite compared to the primary austenite phase [19]. Nitrogen loss, in addition, hinders sufficient austenite to form, which negatively affects the ferrite/austenite phase balance [15,20]. Hence, it is of great importance to control chemical composition, thermal cycling and cooling rate in laser AM of DSS to achieve a desirable microstructure in the deposited component. Post-build treatments, particularly post-build heat treatments, may be necessary to produce balanced ferrite-austenite microstructures and to improve mechanical properties and corrosion resistance of additively manufactured DSS.

Previous studies on laser powder bed fusion (LPBF) of DSS resulted in an almost fully ferritic microstructure after deposition [21–24]. In all studied cases, a post-build heat treatment was needed to balance the ferrite-austenite ratio. Despite lower cooling rates, the unbalanced microstructure is also a challenge in wire-arc additive manufacturing (WAAM) of DSS which has attracted considerable research attention for its high deposition rate and affordable equipment [25–34].

Literature on LMDw processing of DSS is limited. Valiente et al. [16] reported on DSS LMDw microstructure in both the as-deposited (AD) and heat-treated (HT) conditions. The AD microstructure consisted of around 35% austenite, while post heat treatment increased the austenite content to approximately 54%. This study was extended by Baghdadchi et al. [2] to the production of multi-bead and multi-layer blocks, aiming at enabling fabrication of high-quality and high-performance DSS components. The same authors showed in subsequent work that LMDw can produce DSS components with promising mechanical properties in both the AD and HT conditions [35]. For additively manufactured DSS by LMDw, however, the corrosion resistance has not been studied yet and only limited results have been reported on the corrosion resistance of LPBF components [36,37]. By performing polarization measurements in 0.6 M and 1.0 M NaCl solutions, it has been indicated that the as-built ferritic microstructure from LPBF showed no significant difference in corrosion resistance at room temperature as compared to the heat-treated LPBF [37]. However, critical pitting temperature (CPT) measurements by Haghdadi et al. [37] found that the CPT is lower in as-built condition (47 °C) as compared to after post-AM heat treatment (61 °C). Since there is no such data for LMDw of DSS, the present study aims to fill this gap and contribute to an understanding of the relationship between microstructure, chemical composition, and pitting corrosion resistance of DSS additively manufactured by LMDw after deposition and subsequent heat treatment.

2. Experimental

2.1. Materials

Duplex stainless steel (DSS) type 2205 (UNS S32205) with the thickness of 10 mm was used as the build substrate. The DSS type 2209 (EN ISO 14343-A: G 22 9 3 N L) solid wire (1.2 mm diameter) was used as feedstock material. Table 1 lists the chemical composition as given by the material manufacturer certificate.

2.2. Laser metal deposition with wire of the cylinder

Fig. 1-a shows the laser metal deposition with wire (LMDw) system used for this study [16]. The system is comprised of a 6 kW Ytterbium-doped fiber laser, a 6-axis robot, a deposition tool with laser optics, a wire feeder, a control system, and actuators. Spot size was approximately 3.2 mm for out-of-focus deposition with a Gaussian beam power distribution. A hot-wire feed system was used to increase deposition rate by pre-heating the wire using an electrical current. This also aims at improving metal transfer stability, good wettability, and dimensional control [4]. Additionally, a water cooling system was implemented to prevent heat accumulation during fabrication, ensuring stable deposition. A two-section cylinder was deposited by LMDw, as indicated in Fig. 1-b.

Table 1 – Chemical composition of the substrate and wire (wt.%).

	C	Si	Mn	P	S	Cr	Ni	Mo	Cu	N	Fe
Plate	0.016	0.32	1.77	0.027	<0.001	22.77	5.50	3.07	0.21	0.18	Bal.
Wire	0.013	0.52	1.48	0.018	0.001	23.50	8.35	3.40	0.08	0.14	Bal.

More details about the production of the cylinder can be found in Ref. [35]. Images of the LMDw cylinder and its cross-section are shown in Fig. 1-c and d, respectively. Pure (99.99%) argon was used as shielding gas during LMDw.

The prepared LMDw DSS was studied in the as-deposited (AD) and post-build heat-treated (HT) conditions. Heat treatment was performed in a furnace at 1100 °C for 1 h in air followed by water quenching. The goal was to achieve a balanced ferrite-austenite ratio [31] and to dissolve nitrides while avoiding sigma phase formation.

2.3. *Microstructure characterization*

The AD and HT microstructures were examined using light optical and scanning electron microscopy (SEM). Energy dispersive spectroscopy (EDS) in the SEM was used for compositional analysis. The cross-sections were mounted, ground, and polished down to 0.05-μm using alumina suspension. Optical microscopy was performed on a Zeiss Axio Imager.M2m optical microscope. Two different etchants were used s: (i) Modified Beraha (60 ml water, 30 ml HCl, 0.7 g potassium bisulfite) for 12 s for color etching, and (ii) oxalic acid electrolytic etch at 4 V for 10 s. For SEM, backscattered electron (BSE) imaging and EDS analysis were performed just after polishing. The electron beam energy was 18 keV, and the probe current was 1.2 nA for SEM/EDS analysis. For EDS analysis, the contents of alloying elements were measured in both ferrite and austenite in the as-deposited and heat-treated conditions via map and point analysis. For the point analysis, the average of two measurements is reported for each phase. Phase fraction analysis was done using image analysis in ImageJ software [39].

2.4. *Electrochemical pitting corrosion testing*

Samples with a surface area of approximately 1 cm^2 were extracted perpendicular to the build direction in the AD and HT conditions (Fig. 2). Samples were extracted to capture the different microstructures as follows.

1. Cylinder outer surface with primarily as-deposited (non-reheated) microstructure (OS-AD)
2. Cylinder bulk with reheated as-deposited microstructure (B-AD)
3. Cylinder with post-build heat-treated microstructure (HT)

Note that care was taken that the selected sample surfaces not include any obvious defect such as pores or lack of fusion defects. A copper wire was spot welded to the back of the samples to create an electrical contact prior to embedding the samples in epoxy resin. Testing surfaces were then ground with SiC papers down to 4000 grit, rinsed in ethanol and distilled water. Two different electrochemical tests were performed: cyclic potentiodynamic polarization (CPP) according to ASTM G61 [40], and critical pitting temperature (CPT) according to ASTM G150 [41].

The CPP measurements were performed in 1.0 M NaCl solution in a 5-port electrochemical cell consisting of an Ag/AgCl-4MKCl reference electrode (Accumet), a Pt-coated Ti mesh as the counter electrode, and the test sample as the

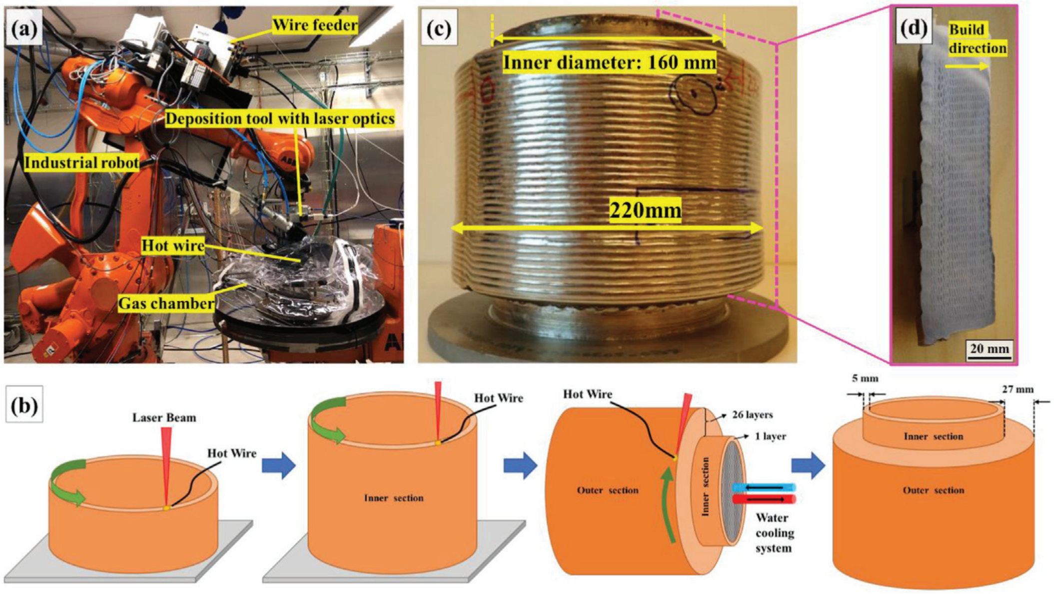

Fig. 1 – a) Laser metal deposition with wire setup, b) procedure of LMDw for fabrication of duplex stainless steel cylinder [35], c) additively manufactured cylinder, and d) cross-section of the cylinder.

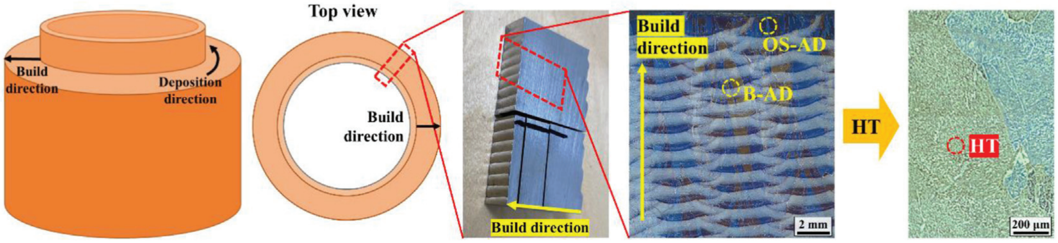

Fig. 2 – Schematic of sample extraction from LMDw DSS for corrosion test: (1) Cylinder outer surface with primarily as-deposited (non-reheated) microstructure (OS-AD); (2) cylinder bulk with reheated as-deposited microstructure (B-AD); and (3) cylinder with post build heat-treated microstructure (HT).

working electrode. Testing was performed at room temperature. The solution concentration was preserved through a water-cooled condenser at 25 °C, and the cell was deaerated with nitrogen gas, including a 1-h period prior to each test to ensure complete deaeration. The corrosion test setup can be seen in Fig. 3. For CPP, a Gamry Instruments potentiostat (Gamry Instruments) was used to step up the potential at a scan rate of 0.167 mV/s from −0.2 V below the open circuit potential (E_{OC}). At a current density of 0.1 mA/cm^2 the scan direction was reversed and the potential was stepped down to −0.2 V below the E_{OC}. Samples were exposed to the open-circuit potential for 30 min, or until E_{OC} stability, prior to the start of the measurements. Resulting CPP curve current values were adjusted to reflect the exact sample area.

The CPT measurements were performed in 1.0 M NaCl solution in a closed double-walled electrochemical cell (Fig. 3). The cell included an Ag/AgCl-4MKCl reference electrode (Accumet), a Pt-coated Ti mesh as the counter electrode, the test sample as the working electrode, and a Tempco Pt RTD probe inserted directly adjacent to the sample surface. The double-walled cell was connected to a Poly Science advanced programmable water heater and circulator to incrementally increase the solution temperature from 30 to 100 °C at a rate of ~1 °C/min. Deaeration and condensation were not performed. CPT values were obtained using a potentiostat (Gamry Instruments) running a potentiostatic hold at 750 mV against the reference electrode potential (E_{ref}). The samples were exposed to the open circuit potential for 100 s prior to the potentiostatic hold, and the critical pitting temperature (CPT) was obtained from the temperature extracted from the thermocouple corresponding to a current density value of 100 μA/cm^2. Three measurements were performed for each sample (OS-AD, B-AD, and HT). Optical microscopy was performed on the sample surface after CPT testing to observe pit behavior. Images were taken of the sample surface before and after etching. Samples were polished to 1 μm before etching with 10% oxalic acid.

2.5. *Thermodynamic and kinetic calculations*

Thermodynamic and kinetic calculations were performed using the Calculation of Phase Diagrams (CALPHAD) method. Two different calculations were done with the commercial

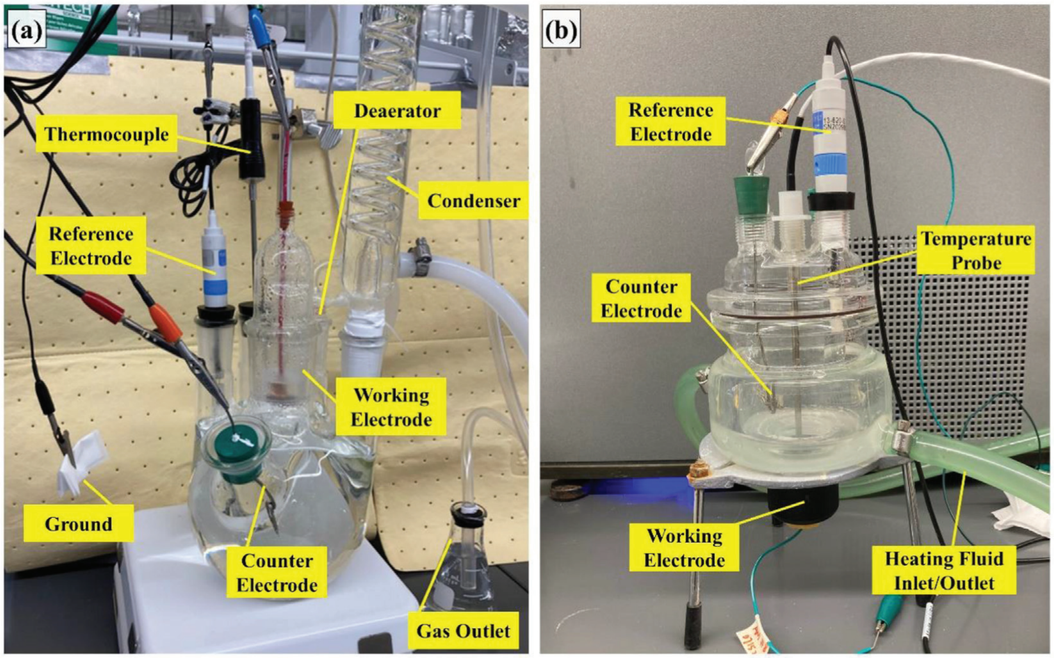

Fig. 3 – a) 5-port electrochemical cell setup for cyclic potentiodynamic polarization (CPP) measurements; and b) double-wall cell setup for critical pitting temperature (CPT) measurements.

software tool Thermo-Calc version 8.5.1.0017 with the TCFE10 database (Thermo-Calc, Stockholm, Sweden):

(i) After fully ferritic solidification of the DSS, ferrite partially transforms to austenite during cooling. The ferrite and austenite phase boundary were simulated using a diffusion calculation in DICTRA (an add-on module to Thermo-Calc software) with the MOBFE5 database. The following initial conditions were assumed/defined for this calculation:
  - Only the main alloying elements (23.5% Cr, 8.3% Ni, 3.3% Mo, and 0.11% N, all wt.%) were considered in the calculation.
  - Based on the equilibrium phase diagram calculated in Thermo-Calc (Fig. 4-a), the calculation started from a fully ferritic microstructure at 1400 °C. During cooling to 1000 °C in 0.5 s the austenite phase forms at the ferrite grain boundary.
  - Based on optical micrographs, the width of the ferrite was assumed to be 10 μm and austenite starts to form with a planar interface from the left side of the ferrite (Fig. 4-b).

(ii) The composition of the ferrite and austenite phases after heat treatment was calculated to evaluate the partitioning of alloying elements. For this calculation, it was assumed that after 1 h at 1100 °C the system approaches equilibrium. The initial alloying element contents used for this calculation were measured by OES analysis (Table 2) and the nitrogen content was measured by combustion analysis [35].

3. Results

3.1. Microstructure characterization

In this section, results from microstructure characterization of the LMDw DSS cylinder are presented for the as-deposited condition, and after post-build heat treatment at 1100 °C for 1 h with subsequent water quenching.

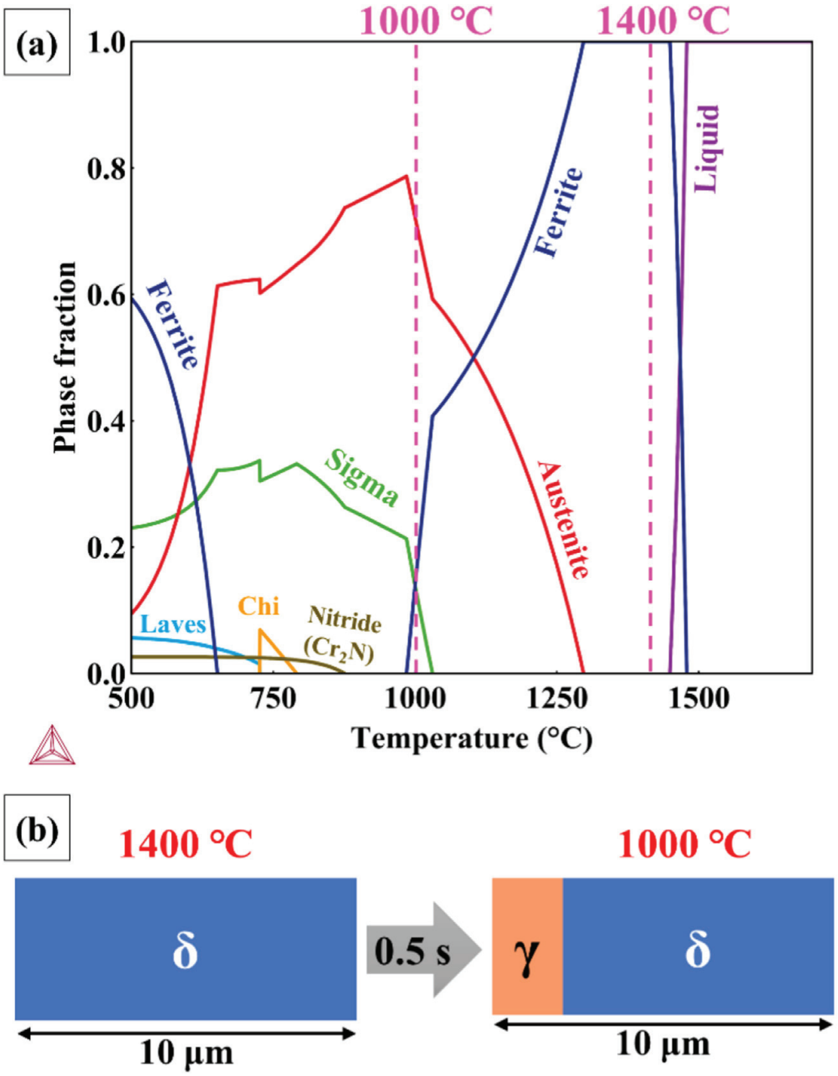

Fig. 4 – a) Equilibrium phase diagram for DSS composition (Table 2) as calculated by Thermo-Calc software, and b) schematic of setup for simulation of ferrite to austenite transformation in DICTRA.

Table 2 – Chemical composition of the LMDw DSS cylinder [35].

C	Si	Mn	P	S	Cr	Ni	Mo	Cu	N	Fe	PREN
0.014	0.48	1.42	0.018	0.002	23.54	8.30	3.32	0.06	0.11	Bal.	36.26

The AD microstructure of DSS additively manufactured by LMDw is presented in Fig. 5-a. In this macrograph, etched with modified Beraha reagent, the dark phase represents ferrite, while the bright phase corresponds to austenite. The multi-bead, multi-layer processing results in two dominant microstructures: (i) predominantly ferritic regions with a small amount of primary austenite (around 2%) that forms primarily along ferrite grain boundaries (Fig. 5-b), and (ii) reheated regions with a high fraction of secondary austenite (up to 33 ± 3%) (Fig. 5-c). In DSS, the austenite that forms during initial cooling after solidification is called primary austenite, while the austenite that forms due to additional reheating and cooling cycles is called secondary austenite. Some small pores and possibly lack of fusion defects between individual beads were observed. Defects are considered a major challenge in AM, for example enabling crack initiation [45]. The few pores and lack of fusion defects observed in this work are consistent with previous studies on laser metal deposition of stainless steel wire [46]. As indicated earlier, care was taken not to include defects in the sample surfaces extracted for corrosion testing. Future studies should explore the role of defect on corrosion behavior specifically.

As can be seen in Fig. 6-a, the electrolytic etching with oxalic acid revealed the presence of clusters of small black precipitates inside the ferrite matrix which are interpreted as chromium nitrides [9,10,16]. Nitride-free zones were also observed around the primary austenite (Fig. 6-a) and where the austenite spacing is low (Fig. 6-b). While during deposition, austenite could only be formed at the ferrite/ferrite grain boundary, reheating due to deposition of the following bead caused the formation of Widmanstätten and intragranular austenite. In addition, both nitrides and secondary austenite formed on the ferritic matrix with relatively higher austenite spacing.

The LMDw DSS after post-build heat treatment at 1100 °C for 1 h is shown in Fig. 7. The microstructure is homogeneous across the built with relatively equal fractions of ferrite and austenite. An austenite percentage of 50 ± 1% was measured via image analysis including grain boundary, Widmanstätten, and intragranular austenite.

3.2. *Chemical composition analysis*

The BSE-SEM images and EDS maps of the DSS produced by LMDw in AD and HT conditions are shown in Fig. 8. In both maps, the right side of the map is the ferrite phase, and the left side is the austenite phase. In the as-deposited condition (Fig. 8-a), EDS analysis reveals that the content of substitutional alloying elements (Cr, Mo, and Ni) is similar in the ferrite and austenite phases. Nitrogen, in contrast, is slightly enriched in the austenite. After heat treatment, the BSE image and EDS map (Fig. 8-b) indicate partitioning of substitutional alloying elements towards the equilibrium condition, i.e., Cr and Mo are enriched in the ferrite phase, while Ni is enriched in the austenite phase.

Data from EDS point analysis is presented in Table 3 and reiterates the results obtained from mapping. The ferrite and austenite compositions are very similar in the as-deposited condition. Note that EDS is generally a qualitative and semi-quantitative measurement technique, in particular the quantification of nitrogen is not possible from EDS due to its low atomic number. Therefore, the nitrogen values provided in Table 3 only serve as an indication that the nitrogen level is higher in the austenite phase as compared to the ferrite phase. In the heat-treated condition, Cr and Mo are concentrated in the ferrite phase, while Ni and N are enriched in the austenite phase.

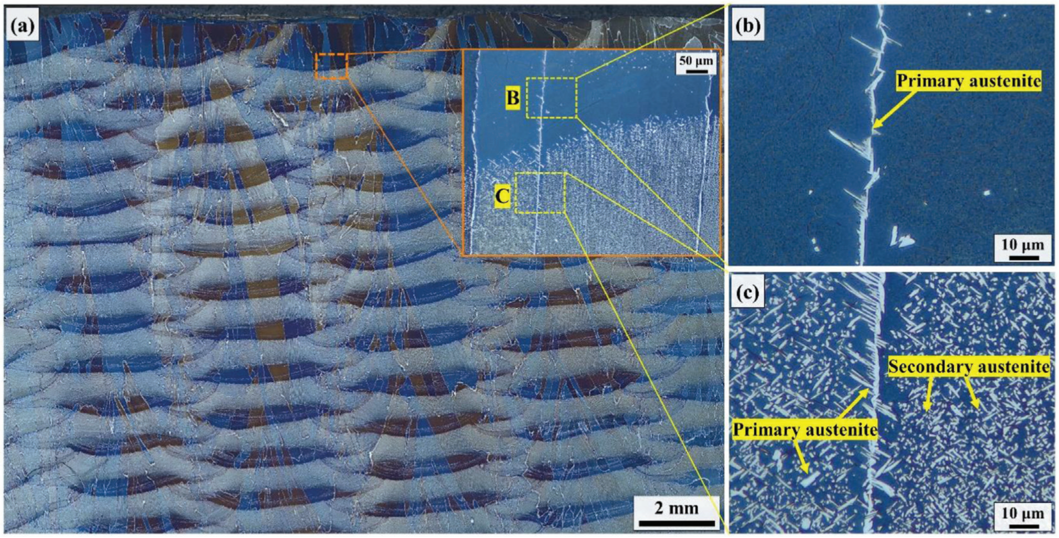

Fig. 5 – a) Optical micrograph of the as-deposited microstructure of the LMDw DSS cylinder showing b) predominantly ferritic regions with a small fraction of primary austenite, and c) reheated regions with a high fraction of secondary austenite.

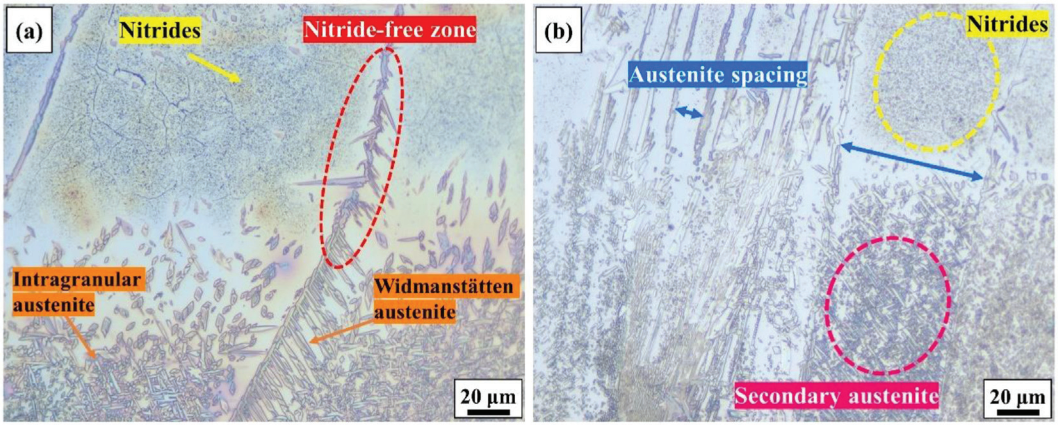

Fig. 6 – Microstructures of the as-deposited LMDw DSS electrolytically etched with oxalic acid: a) Nitride formation inside of ferrite grains and nitride-free zones close to grain boundary austenite; and b) formation of either nitrides or secondary austenite in areas with relatively larger austenite spacing. The bottom region in both images shows the reheated microstructure with a high amount of secondary austenite, while the top (non-reheated) regions are predominantly ferritic with nitrides and little primary austenite.

3.3. *Thermodynamic and kinetic calculations*

The results from diffusion calculations are presented in Fig. 9 and Table 4. It is assumed that austenite forms from the ferrite phase during cooling from 1400 °C to 1000 °C in 0.5 s. The width of the austenite grain is about 1–2 μm, which is in the range of what was seen for the size of primary grain boundary austenite in optical microscopy (Fig. 5-c). The contents of Cr, Mo, and Ni are around 23.5%, 3.3%, and 8.3% in austenite which are similar to the ferritic matrix. However, N increases from 0.04% in ferrite to 0.45% in austenite, demonstrating diffusion of N from ferrite to austenite. It should be noted that the significant changes and sharp peaks in the content of Cr, Mo, and Ni at the ferrite-austenite boundary are due to the nature of the moving boundary type DICTRA simulation. DICTRA keeps the phase boundary in equlibrium at all times during the simulation. This implies that the chemical compositions on either sides of the boundary must align with the tie-line chemistries for ferrite and austenite, even as the temperature is rapidly decreasing.

The predicted ferrite and austenite composition from the equilibrium calculation at 1100 °C are presented in Table 4. Ni and N are predicted to be enriched in austenite, while Cr and Mo are predicted to be accommodated in the ferrite phase. Considering the elemental compositions obtained from the thermodynamic and kinetic calculations, the pitting resistance equivalent number (PREN = % Cr + 3.3% Mo + 16% N) [42] was calculated for the ferrite and austenite phase in the as-deposited and heat-treated conditions and included in Table 4. These calculations suggest that the austenite phase has a

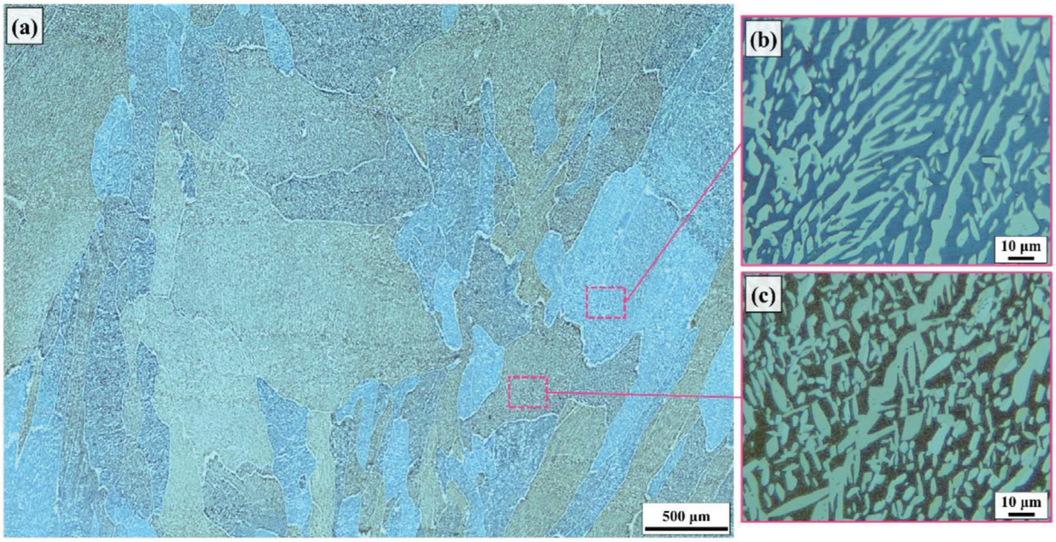

Fig. 7 – LMDw DSS microstructure after heat treatment at 1100 °C for 1 h at two different magnifications showing homogeneous distribution and balanced fractions of ferrite and austenite.

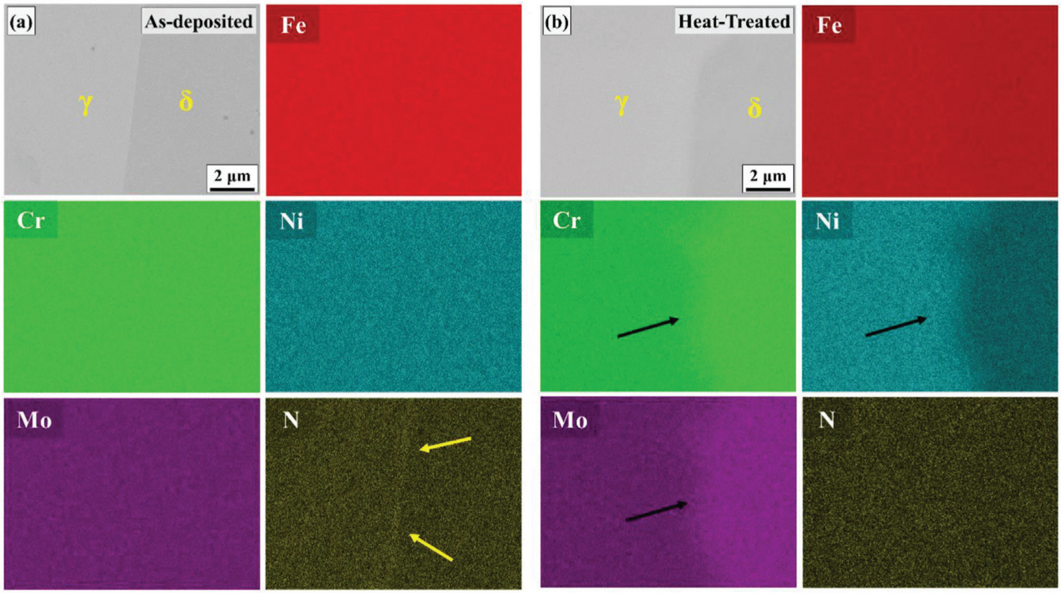

Fig. 8 – BSE images and SEM-EDS maps of LMDw DSS: a) in as-deposited condition, and b) after heat treatment. The high cooling rate of LMDw suppresses the diffusion of substitutional elements (Cr, Mo, Ni). Only the N content is different in the as-deposited austenite and ferrite phase. Heat treatment (1 h at 1100 °C) provided enough time at elevated temperatures for element distribution in ferrite and austenite toward equilibrium composition.

higher PREN value compared to ferrite in the as-deposited condition. While after heat treatment, the ferrite phase has a higher PREN value as compared to the austenite.

3.4. *Corrosion resistance*

Fig. 10-a shows representative cyclic potentiodynamic polarization (CPP) curves for the three different LMDw DSS samples (OS-AD, B-AD, and HT) recorded in 1.0 M NaCl solution at room temperature. All samples exhibited a wide passive range and a passive current density during the forward scan of less than 10^{-4} A/cm^2, indicating the formation of a passive film on the sample surface. At anodic potentials higher than 1.1 $V_{Ag/AgCl}$, the current density sharply increased for all samples due to a combination of oxygen evolution and transpassive dissolution resulting from the generation of Cr^{6+} and Mo^{6+} species. During the reverse scan, the anodic current densities decreased significantly for all samples. The cross-over potential from anodic to cathodic current was observed at approximately 0.7 $V_{Ag/AgCl}$. Because CPP curves are plotted in terms of the log of absolute current density for convenience of visualization, the cross-over potential is indicated by the extremely low current density inflection point (essentially, the current changes sign at this potential). This high cross-over potential during the reverse scan indicates that the samples were covered by a stable passive film that resulted in low anodic current densities. The negative hysteresis (i.e., the current during the reverse scan is less than that during the forward scan) in the CPP curves of all samples indicates uniform corrosion in the transpassive region rather than localized (pitting) corrosion. It can be concluded that the polarization measurements at room temperature did not show any significant difference in pitting corrosion resistance between the OS-AD, B-AD and HT samples in terms of pitting potential and passive current density.

Table 3 – Composition of the ferrite and austenite phase from SEM/EDS point analysis in as-deposited condition and after heat treatment. Values are given as averages from two separate measurements.
(*) Note that quantification of N is not possible from EDS data; values are given only as an indication that N content is higher in the austenite phase as compared to the ferrite phase.

		Cr	Ni	Mo	Mn	N*
As-Deposited	Ferrite	24.4	8.3	3.4	1.4	0.0
	Austenite	24.2	8.4	3.4	1.4	0.1
Heat-Treated	Ferrite	26.6	6.4	4.2	1.4	0.0
	Austenite	21.5	10.5	2.6	1.6	0.2

Representative critical pitting temperature (CPT) measurements in 1.0 M NaCl solution with a temperature ramp of ~1 °C/min are presented in Fig. 10-b. The CPT represents the minimum temperature at which stable pits start to grow, evidenced by the sharp increase in current density observed as a static potential and temperature ramp are applied. A current density threshold of 100 μA/cm^2 was used to isolate critical temperatures. The OS-AD sample showed the lowest critical temperature at an average value of 60 ± 0.6 °C. The B-AD and HT samples exhibited higher critical temperatures with an average of 73 ± 0.6 °C and 68 ± 0.9 °C, respectively.

Fig. 11 shows images from optical microscopy of the CPT test sample surfaces. The OS-AD sample exhibited typical pitting corrosion behavior manifested as clustered pits (Fig. 11-a). In contrast, no substantial pitting was observed on the B-AD and HT sample surfaces, however, crevice corrosion occurred near the edge of the mount. Fig. 11-b shows corrosion on the B-AD sample surface along the leading edge of the crevice. Preferential corrosion occurred in the ferritic regions of the

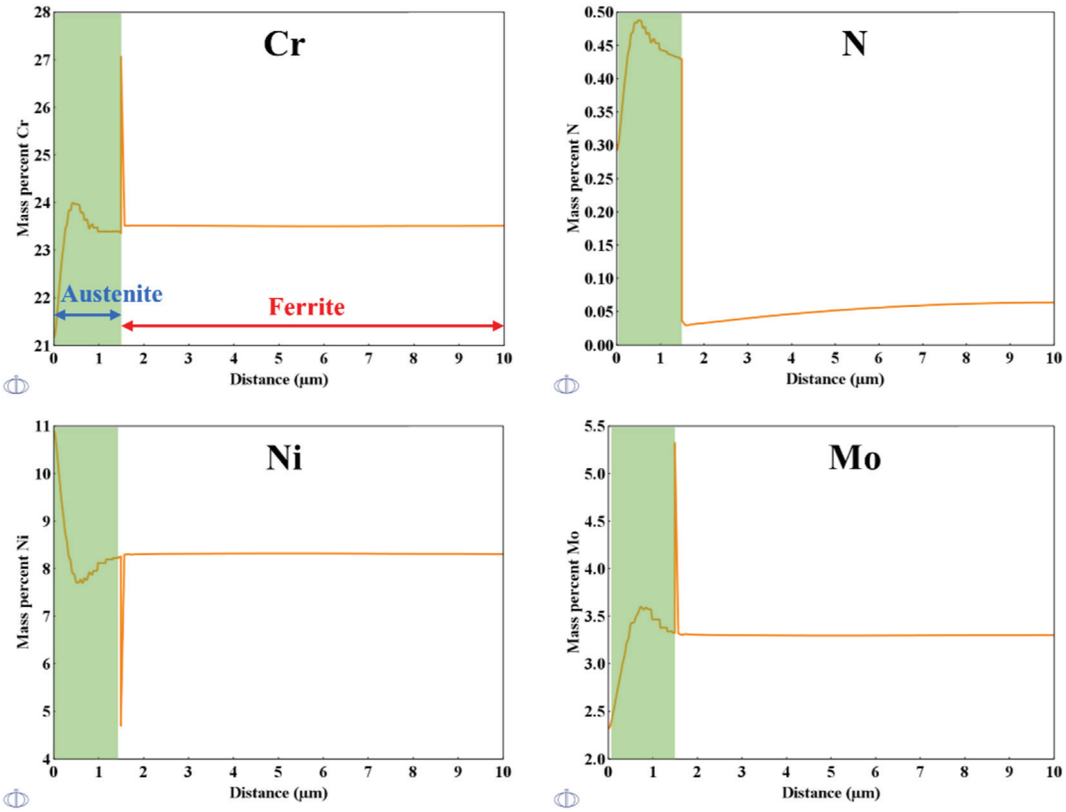

Fig. 9 – Elemental partitioning between ferrite and austenite after cooling from 1400 to 1000 °C in 0.5 s. The high cooling rate of LMDw restricts the diffusion of substitutional elements (Cr, Ni, and Mo). Nitrogen (interstitial) is the only element that diffuses between ferrite and austenite and gets enriched in the austenite phase.

Table 4 – Predicted chemical composition of ferrite and austenite phase from thermodynamic and kinetic calculations in Thermo-Calc, and corresponding pitting resistance equivalent number (PREN).

	Phase	Cr	Ni	Mo	Mn	N	PREN
Dictra calculation- ferrite to austenite transformation	Ferrite	23.6	8.3	3.3	1.4	0.05	35.29
	Austenite	23.5	8.3	3.3	1.4	0.45	42.39
Equilibrium calculation at 1100 °C	Ferrite	26.6	5.8	4.2	1.2	0.038	41.07
	Austenite	20.8	10.3	2.5	1.5	0.17	31.77

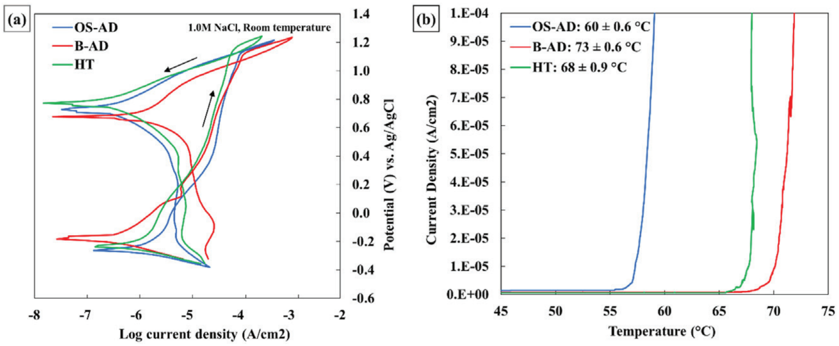

Fig. 10 – a) Cyclic potentiodynamic polarization (CPP) curves obtained in 1.0 M NaCl solution at room temperature and b) critical pitting temperature (CPT) curves in 1.0 M NaCl solution with a temperature ramp of ~1 °C/min for the as-deposited outer surface (OS-AD), bulk (B-AD) and heat-treated (HT) LMDw DSS samples. The average values for CPT along with the corresponding standard deviations measured from at least three measurements for each sample are also included.

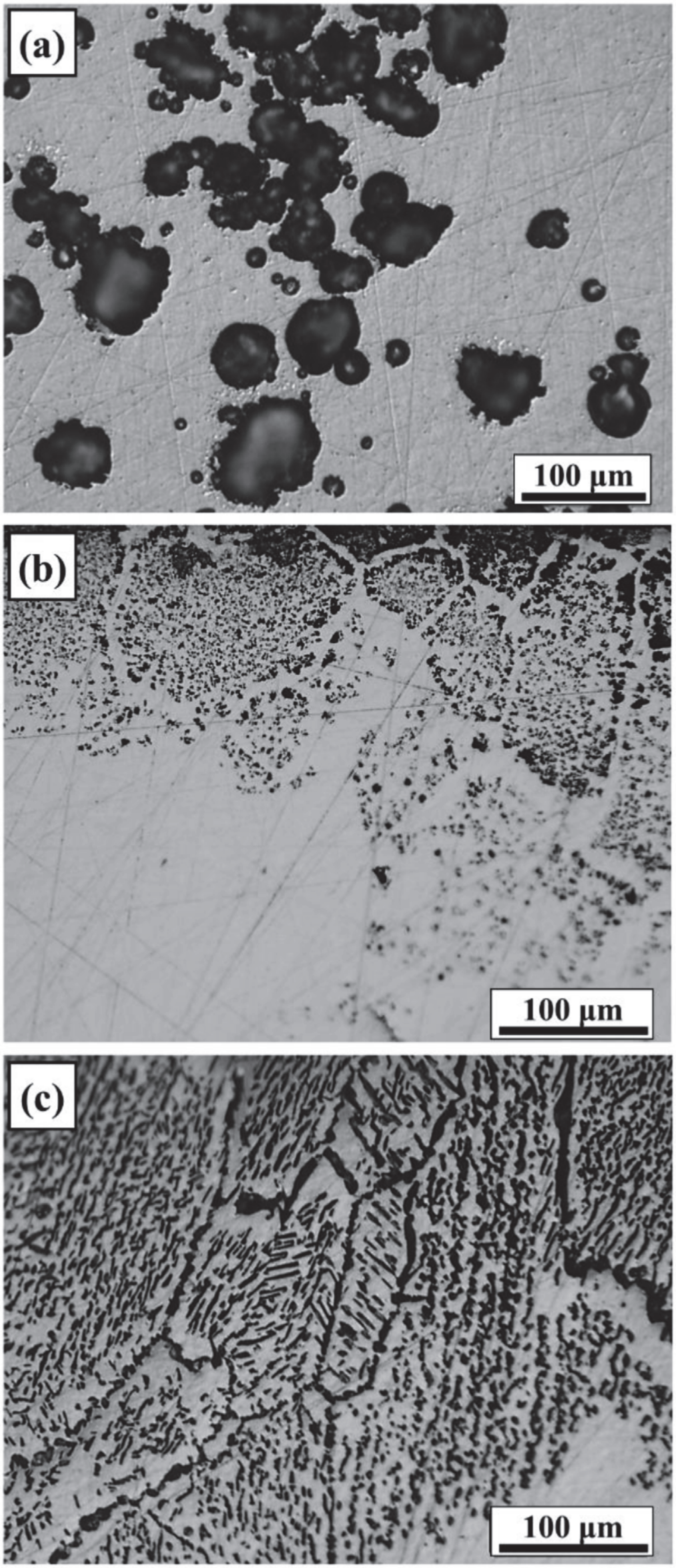
(a)
100 μm
(b)
100 μm
(c)
100 μm

grain interior, while the secondary austenite and grain boundary austenite remained intact. Crevice corrosion near the edge of the mount in the HT sample is shown in Fig. 11-c. In contrast to what was seen in the B-AD sample, corrosion in the HT sample occurred preferentially along the grain boundary austenite and intragranular austenite.

To further differentiate between the three sample conditions and evaluate the effect of the different microstructures on corrosion resistance, additional CPP curves were obtained in 1.0 M NaCl solution at elevated temperature (50 ± 2 °C) (Fig. 12). For testing at elevated temperatures, the electrochemical cell was placed on a hot plate (Fisher Isotemp) to maintain a temperature of 50 °C (±2 °C) throughout the test. The temperature was measured by a K-type thermocouple inserted into the cell. Contrary to what was observed at room temperature, the CPP curves in Fig. 12 show a well-defined passive current density below or at around 10^{-6} A/cm$^{2.}$ A positive hysteresis loop associated with pitting corrosion is observed, i.e. the reverse scan current is higher than the forward scan current. The pitting potential (E_{pit}) is the potential above which stable pits initiate rapidly. It is characterized by a sudden increase in current density as the potential is stepped up. The potential below which stable pits cease to grow is termed the repassivation potential (E_{rp}), which is taken when the hysteresis loop is complete. and the current density reaches the passive current density set at a static value of 10^{-6} A/cm^2. As can be seen in Fig. 12, the B-AD and HT samples exhibit a different behavior than the OS-AD sample when tested at elevated temperature (50 ± 2 °C). The OS-AD sample shows the lowest average pitting potential (72 ± 8 mV$_{Ag/AgCl}$) while the B-AD and HT samples have significantly higher average pitting potentials of 643 ± 178 mV$_{Ag/AgCl}$ and 826 ± 70 mV$_{Ag/AgCl,}$ respectively. The OS-AD and HT samples exhibit the highest repassivation potential with an average of −130 ± 40 mV$_{Ag/AgCl}$ and −134 ± 75 mV$_{Ag/AgCl}$, respectively. The B-AD sample showed the lowest average repassivation potential of −165 ± 34 mV$_{Ag/AgCl}$.

4. Discussion

Duplex stainless steel (DSS) cylinder was produced by laser metal deposition with wire (LMDw) and subsequently heat treated at 1100 °C for 1 h. In this section, the relationship between microstructure, chemical composition, and corrosion resistance are discussed in the as-deposited (AD) and heat-treated (HT) conditions.

4.1. *As-deposited and heat-treated laser metal deposited microstructure*

In AD condition, the microstructure was inhomogeneous including regions with almost fully ferritic microstructure and regions with a high fraction of secondary austenite. Upon deposition, the DSS solidifies as 100% ferrite, and then the ferrite phase partially transforms into austenite [2]. In LMDw, the high cooling rate (10^3–10^5 °C/s) [43,44] of the process restricts sufficient ferrite to austenite transformation, and therefore the structure remains predominantly ferritic with a low austenite fraction. In addition, austenite formation on cooling is limited due to nitrogen loss during LMDw processing [2,15,16]. Due to the limited amount of austenite, nitrogen is supersaturated in the ferrite phase. Nitrogen solubility in ferrite decreases with the decrement in temperature, which leads to the precipitation of chromium-rich nitrides inside the ferrite grains (Fig. 6). Both nitrides and secondary austenite formed in the ferritic region with higher austenite spacing. In regions with low austenite spacing, nitrogen diffuses into the austenite due to the short diffusion path, and subsequently, there is no nitrogen available for nitride formation. Reheating due to the deposition of subsequent beads and layers increases the amount of austenite because of further growth of existing (primary) austenite, formation of Widmanstätten austenite, and nucleation of intragranular austenite (Fig. 5-c). In the high temperature heat-affected zone of individual beads, reheating dissolves the chromium-rich nitrides in the ferrite matrix and provides time at elevated temperatures for nitrogen diffusion and subsequent secondary austenite formation. Fig. 6-a and 6-b show the high amount of secondary austenite in the high temperature heat-affected zone (bottom region) as compared to the predominantly ferritic structure with finely dispersed nitrides and little primary austenite (top region). After 1 h heat treatment at 1100 °C, however, the microstructure was homogeneous with balanced fractions of ferrite and austenite. Heat treatment, in addition, caused dissolution of chromium nitrides, and the growth and coarsening of both primary and secondary austenite.

4.2. *Partitioning of alloying elements in laser metal deposition and post-process heat treatment*

The SEM-EDS chemical composition analysis revealed that in AD condition, ferrite and austenite phases have almost similar contents of alloying elements and nitrogen is the only element differs in these two phases. In LMDw, the implementation of a water-cooling system resulted in a notably elevated cooling rate. The high cooling rate severely suppresses the diffusion and the segregation of substitutional alloying elements. Nitrogen as a fast-diffusing interstitial element is able to diffuse to the austenite during initial cooling from solidification and during subsequent reheating cycles. However, after heat treatment, the ferrite-stabilizer elements like Cr and Mo were partitioned in ferrite and the austenite-promoting elements like Ni were distributed in austenite. The heat treatment provided enough time at elevated temperatures for the diffusion and partitioning of alloying elements in ferrite and austenite.

Fig. 11 – Optical microscopy images of CPT test sample surfaces: (a) Clustered corrosion pits in the outer-surface as-deposited (OS-AD) sample, (b) crevice corrosion near the edge of the mount of the bulk as-deposited (B-AD) sample with preferential corrosion in the grain interior; and (c) crevice corrosion near the edge of the mount of the heat-treated (HT) sample with preferential corrosion along the grain boundaries and inside the grains.

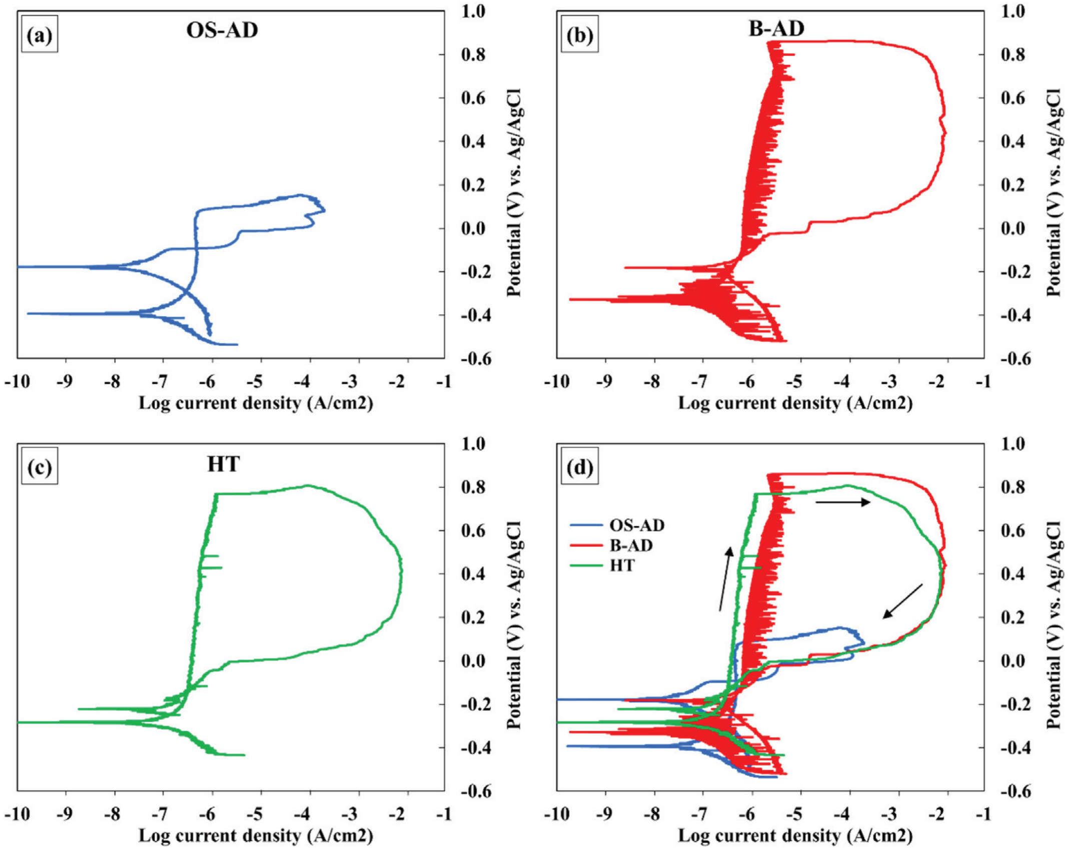

Fig. 12 – Cyclic potentiodynamic polarization (CPP) curves for a) the as-deposited outer surface (OS-AD), b) bulk (B-AD), and c) heat-treated (HT) LMDw DSS samples, as well as d) a comparative graph. All obtained in a 1.0 M NaCl solution at an elevated temperature of 50 ± 2 °C.

The thermodynamic calculation via Dictra for austenite formation during deposition, similarly, demonstrated the contents of Cr, Mo, and Ni are similar in ferrite and austenite. However, nitrogen diffuses in austenite. This is in good agreement with what was measured experimentally on the as-deposited LMDw DSS using SEM-EDS (Table 3). Nitrogen is the only element that diffuses from the ferritic matrix to the austenite that formed at the ferrite/ferrite grain boundary during initial cooling from solidification. In addition, according to equilibrium calculation at 1100 °C, the Ni and N are predicted to be enriched in austenite, while Cr and Mo are predicted to be accommodated in the ferrite phase. The compositions of ferrite and austenite are close to what was measured experimentally in the heat-treated LMDw DSS using SEM/EDS, indicating that the system is approaching equilibrium after 1 h at heat treatment temperature.

4.3. *Effect of laser metal deposited microstructure on corrosion resistance*

Corrosion testing at room temperature did not show any significant differences in pitting corrosion resistance between the DSS samples produced by LMDw in AD and HT conditions, despite significant differences in the microstructures. All samples showed a high corrosion resistance with a wide passive region and stable surface up to 1.1 $V_{Ag/AgCl}$, at which transpassive dissolution occurred associated with uniform corrosion rather than pitting. The lack of a hysteresis loop in the CPP curves and the absence of pitting on the sample surface for all samples indicates that the LMDw samples in AD condition has comparable corrosion performance at room temperature and at comparable chloride concentration relative to the HT sample. This is in good agreement with previous work on LPBF of 22% Cr DSS, which showed almost fully ferritic as-build microstructures that had comparable corrosion resistance at room temperature as compared to the HT condition [38,39]. Results from the present study show that the high cooling rates in LMDw, albeit somewhat lower than in LPBF, similarly create a predominantly ferritic structure in the last deposited layer (i.e., the OS-AD sample). At room temperature, the numerous chromium-rich nitrides inside this predominantly ferritic microstructure (Fig. 6-a) do not appear to act as initiation sites for pitting corrosion. From arc welded DSS, it is known that Cr-depleted regions around chromium-rich nitrides cause initiation of localized corrosion if exposed to aggressive environments [47]. However, nitride size, distribution, and local chemical environment also affect their susceptibility to serve as corrosion initiation sites [48]. Hadghdadi et al. [37] reported that nano-sized chromium-rich nitrides did not cause localized corrosion in as-deposited LPBF DSS when tested in 1.0 M NaCl at room temperature. In addition, it was shown that while Cr-depleted regions were present around the Cr_2N using atom probe tomography, the level of Cr stayed above the critical level for corrosion resistance i.e., 13 wt% Cr. The bulk as-deposited (B-AD) LMDw DSS in this study exhibited a mixed microstructure of predominantly ferritic regions, and reheated regions that contain up to 33 ± 3% austenite due to partial reheating of the underlying layer during the multi-layer deposition process. During reheating, nitrides get dissolved in the ferritic matrix, and subsequently secondary austenite forms. Diffusion of substitutional elements during reheating cycles is limited, hence the austenite phase is very similar in composition of the substitutional alloying elements compared to the ferrite matrix but has a higher nitrogen content. Nitrogen is a fast diffuser and can easily be redistributed even under the high cooling rate conditions of LMDw. After the heat treatment, a balanced austenite-ferrite microstructure is formed, and the chromium-rich nitrides are dissolved. Moreover, Cr and Mo are accommodated in the ferrite phase, while Ni and N are enriched in the austenite phase.

As described, the differences in microstructures in terms of phase fraction, elemental distribution, and presence of chromium-rich nitrides in the as-deposited and heat-treated LMDw DSS did not result in any significant differences in corrosion resistance at room temperature. However, differences in corrosion resistance were apparent from the critical pitting temperature (CPT) measurements [37,47,48]. The critical temperature was lowest (60 ± 0.6 °C) for the OS-AD sample, which showed evidence of clustered pits on the sample surface (Fig. 11-a). Chromium-rich nitrides in the predominantly ferritic microstructure may have served as initiation sites for pitting. This would indicate the importance of temperature on their susceptibility to serve as initiation sites for pitting corrosion [49,50], as these nitrides remained stable during CPP room temperature testing. Also, the high cooling rate and the resulting depletion of N may have rendered the ferrite matrix susceptible to pit initiation. The B-AD and HT samples achieved critical temperatures of 73 ± 0.6 °C and 68 ± 0.9 °C, respectively, and therefore showed higher critical temperatures as compared to the OS-AD sample. However, the B-AD and HT samples did not show typical corrosion pits on the sample surface, but crevice corrosion occurred near the edge of the mounted samples. Interestingly the regions in which preferential corrosion occurred in the microstructure differed between the B-AD and HT samples. On the B-AD sample surface, corrosion occurred preferentially in the ferrite phase of the grain interior, while the grain boundary austenite and secondary austenite remained intact (Fig. 11-b). Selective dissolution of ferrite above the CPT has been previously reported in 22% Cr DSS to be due to the depletion of N [38]. The ferrite and austenite phases in the B-AD sample are of similar composition in terms of Cr and Mo, but the ferrite phase is depleted in N, making it more susceptible to dissolution at temperatures above the CPT. In contrast, preferential corrosion in the HT sample occurred in the austenite phase along the grain boundaries and in the grain interior, while the ferrite phase remained intact (Fig. 11-c). The heat treatment resulted in a redistribution of alloying elements toward the equilibrium. In HT condition, the concentration of Cr and Mo is higher in the ferrite. As a result, the austenite becomes the weaker phase, less stable, and more susceptible to corrosion due to the depletion of Cr and Mo. The observed differences in corrosion resistance of the ferrite and austenite phases are in good agreement with the calculated PREN values for the AD and HT conditions (see Table 4). The B-AD and HT samples showed higher critical temperatures than the OS-AD sample, despite exhibiting crevice corrosion. Typically, crevice corrosion leads to a lower critical temperature because of the greater restriction to the access of bulk electrolyte and the resulting maintenance of a concentrated critical solution chemistry in pits within the creviced area. However, the crevices present in the samples were not controlled and may have led to small differences in critical temperatures between the HT and B-AD samples. Nevertheless, the differences between these conditions and the OS-AD condition suggests a strong role of microchemistry on localized corrosion. Future testing should investigate crevice-free configuration to compare the CPT and measure a reproducible critical crevice temperature using controlled crevice devices. It should be noted that practical applications, crevices are difficult to avoid and a critical crevice temperature may be a more conservative measure of the localized corrosion resistance of the duplex stainless steel.

At the elevated temperature (50 ± 2 °C), the occurrence of hysteresis in the CPP curves correlated to localized corrosion of the additively manufactured DSS by LMDw in both AD and HT conditions. Similar to what was observed in the CPT measurements, pitting corrosion occurred on the OS-AD sample surface, while crevice corrosion near the edge of the mount was observed in the B-AD and HT samples. A large difference was observed in the obtained pitting potential. The predominantly ferritic structure in the last deposited layer (OS-AD) showed a significant lower pitting potential as compared to the ferritic-austenitic (roughly 70-30%) structure of the B-AD sample and the balanced ferrite-austenite structure after heat treatment. The increment of the temperature increases the aggressiveness of the test solution, i.e. accelerates the activity of Cl^- and promotes the dissolution of corrosion products. It is hypothesized that, contrary to what was observed at room temperature, chromium-rich nitrides acted as initiation sites for pitting corrosion on the OS-AD sample surface at elevated temperatures [49,50], similar to what was observed at temperatures above the CPT. Moreover, the N depletion of the ferrite phase may have lowered the resistance of the ferrite matrix to pit initiation. A slightly higher repassivation potential was obtained for the OS-AD and HT samples as compared to the B-AD sample. However, the difference in repassivation characteristics between the samples was much less pronounced. The OS-AD sample exhibited a low pitting potential and a small hysteresis. The repassivation potential is a function of the charge passed [51,52]. The B-AD and HT samples showed a much larger hysteresis and therefore a much larger charge passed than the OS-AD sample. A comparison of repassivation potentials under equivalent charge, for example by using the ASTM G-192 [53] procedure, may have shown differences in repassivation potentials.

5. Conclusions

Microstructure, elemental distribution, and corrosion resistance of a DSS cylinder additively manufactured by laser metal deposition with wire (LMDw) were characterized in the as-deposited condition and after a post-process treatment. The results of this study demonstrate how differences in the microstructure in terms of ferrite-to-austenite ratio, distribution of corrosion resistant elements and the presence of nitrides affect the corrosion resistance of DSS additively manufactured by LMDw in AD and HT conditions. The following conclusions can be drawn:

1. As-deposited LMDw microstructure consisted of predominantly ferritic regions with a small fraction of primary austenite (~2%) and numerous chromium-rich nitrides. EDS measurements and Dictra calculation indicated similar Cr, Mo, and Ni content in ferrite and austenite in AD condition. Heat treatment at 1100 °C balanced ferrite and austenite fractions, facilitating diffusion of Cr, Mo to ferrite and Ni, N to austenite.
2. Room temperature CPP measurements revealed no significant difference in corrosion resistance between AD and HT conditions. The observed microstructural variations did not impact the electrochemical response.
3. The AD sample's predominantly ferritic microstructure with chromium-rich nitrides exhibited the lowest CPT at 60 °C, while reheated AD with an increased austenite fraction (up to 33%) and HT samples with a balanced ferrite to austenite microstructure showed higher CPT values (73 °C and 68 °C).

Declaration of competing interest

The authors declare that they have no known competing financial interests or personal relationships that could have appeared to influence the work reported in this paper.

Acknowledgments

The authors would like to thank Prof. Leif Karlsson (University West, Sweden) for his comments and help in this study. Mats Högström (University West, Sweden) and Björn Axelsson (AlfaLaval Tumba AB, Sweden) are also acknowledged for their help in supplying (additively manufacturing) and preparation of the samples. Corrosion testing was performed at the Fontana Corrosion Center at The Ohio State University (USA). Jeremy McNicol (The Ohio State University, USA) is acknowledged for his support with sample preparation and corrosion testing. This project was supported by grants from the Swedish Knowledge Foundation projects SAMw [20170060] and Directed Energy Deposition for Industrial Competitiveness in Additive Manufacturing Technologies (DEDICATE, Dnr.20210094) funded by the Swedish Knowledge Foundation (KK-Stiftelsen, Stiftelsen för kunskaps-och kompetensutveckling)., the NSF/IUCRC Manufacturing & Materials Joining Innovation Center (Ma^{2}JIC) [Award Number 2052747], and i-Weld project H2020-MSCA-RISE-2018 (Project number: 823786). The project was further supported by an ENGIE-Axium Fellowship award provided by The Ohio State University Graduate School.

REFERENCES

[1] Liu L, Xu W, Zhao Y, Lin Z, Liu Z, Dong Y, et al. Tailoring the microstructure and mechanical properties of wire and arc additive manufactured Al–Mg alloy via interlayer friction stir processing. J Mater Res Technol 2023;25:1055–68. https://doi.org/10.1016/j.jmrt.2023.06.053.

[2] Baghdadchi A, Hosseini VA, Valiente Bermejo MA, Axelsson B, Harati E, Högström M, et al. Wire laser metal deposition of 22% Cr duplex stainless steel: as-deposited and heat-treated microstructure and mechanical properties. J Mater Sci 2022;57:9556–75. https://doi.org/10.1007/s10853-022-06878-6.

[3] DebRoy T, Wei HL, Zuback JS, Mukherjee T, Elmer JW, Milewski JO, et al. Additive manufacturing of metallic components – process, structure and properties. Prog Mater Sci 2018;92:112–224. https://doi.org/10.1016/j.pmatsci.2017.10.001.

[4] Kisielewicz A, Thalavai Pandian K, Sthen D, Hagqvist P, Valiente Bermejo MA, Sikström F, et al. Hot-wire laser-directed energy deposition: process characteristics and benefits of resistive pre-heating of the feedstock wire. Metals 2021;11:634. https://doi.org/10.3390/met11040634.

[5] Wang Q, Shi Y, Li X, Wang X, Fan K, Sun R. Additive technology of high-frequency induction-assisted laser wire deposition. Opt Laser Technol 2023;167:109785. https://doi.org/10.1016/j.optlastec.2023.109785.

[6] Moura VS, Lima LD, Pardal JM, Kina AY, Corte RRA, Tavares SSM. Influence of microstructure on the corrosion resistance of the duplex stainless steel UNS S31803. Mater Char 2008;59:1127–32. https://doi.org/10.1016/j.matchar.2007.09.002.

[7] Gunn RN. Duplex stainless steels: microstructure, properties and applications. Uk: Woodhead Publ Sawston; 1997. p. 219.

[8] Sridhar N. Localized corrosion in seawater – a bayesian network based review. Corrosion 2022:4215. https://doi.org/10.5006/4215.

[9] Örnek C, Engelberg DL. Correlative EBSD and SKPFM characterisation of microstructure development to assist determination of corrosion propensity in grade 2205 duplex stainless steel. J Mater Sci 2016;51:1931–48. https://doi.org/10.1007/s10853-015-9501-3.

[10] Pohl M, Storz O, Glogowski T. Effect of intermetallic precipitations on the properties of duplex stainless steel. Mater Char 2007;58:65–71. https://doi.org/10.1016/j.matchar.2006.03.015.

[11] Ezuber HM, El-Houd A, El-Shawesh F. Effects of sigma phase precipitation on seawater pitting of duplex stainless steel. Desalination 2007;207:268–75. https://doi.org/10.1016/j.desal.2006.05.021.

[12] Kim JH, Oh EJ, Lee BC, Kang CY. Effect of aging treatment on impact toughness and corrosion resistance of super duplex stainless steel. J Mater Eng Perform 2016;25:9–14. https://doi.org/10.1007/s11665-015-1816-3.

[13] Tan H, Wang Z, Jiang Y, Han D, Hong J, Chen L, et al. Annealing temperature effect on the pitting corrosion resistance of plasma arc welded joints of duplex stainless steel UNS S32304 in 1.0M NaCl. Corrosion Sci 2011;53:2191–200. https://doi.org/10.1016/j.corsci.2011.02.041.

[14] Kim ST, Lee IS, Kim JS, Jang SH, Park YS, Kim KT, et al. Investigation of the localized corrosion associated with

phase transformation of tube-to-tube sheet welds of hyper duplex stainless steel in acidified chloride environments. Corrosion Sci 2012;64:164–73. https://doi.org/10.1016/j.corsci.2012.07.014.

[15] Baghdadchi A, Hosseini VA, Hurtig K, Karlsson L. Promoting austenite formation in laser welding of duplex stainless steel—impact of shielding gas and laser reheating. Weld World 2020;65:499–511. https://doi.org/10.1007/s40194-020-01026-7.

[16] Valiente Bermejo MA, Thalavai Pandian K, Axelsson B, Harati E, Kisielewicz A, Karlsson L. Microstructure of laser metal deposited duplex stainless steel: influence of shielding gas and heat treatment. Weld World 2021;65:525–41. https://doi.org/10.1007/s40194-020-01036-5.

[17] Karlsson L, Arcini H. Low energy input welding of duplex stainless steels. Weld World 2012;56:41–7. https://doi.org/10.1007/BF03321380.

[18] Karlsson L. Welding duplex stainless steels - a review of current recommendations. Weld World 2012;56:65–76. https://doi.org/10.5937/zzk1802065k.

[19] Nilsson JO, Karlsson L, Andersson JO. Secondary austenite for mation and its relation to pitting corrosion in duplex stainless steel weld metal. Mater Sci Technol 1995;11:276–83. https://doi.org/10.1179/mst.1995.11.3.276.

[20] Hosseini VA, Wessman S, Hurtig K, Karlsson L. Nitrogen loss and effects on microstructure in multipass TIG welding of a super duplex stainless steel. Mater Des 2016;98:88–97. https://doi.org/10.1016/j.matdes.2016.03.011.

[21] Davidson K, Singamneni S. Selective laser melting of duplex stainless steel powders: an investigation. Mater Manuf Process 2016;31:1543–55. https://doi.org/10.1080/10426914.2015.1090605.

[22] Hengsbach F, Koppa P, Duschik K, Holzweissig MJ, Burns M, Nellesen J, et al. Duplex stainless steel fabricated by selective laser melting - microstructural and mechanical properties. Mater Des 2017;133:136–42. https://doi.org/10.1016/j.matdes.2017.07.046.

[23] Saeidi K, Kevetkova L, Lofaj F, Shen Z. Novel ferritic stainless steel formed by laser melting from duplex stainless steel powder with advanced mechanical properties and high ductility. Mater Sci Eng, A 2016;665:59–65. https://doi.org/10.1016/j.msea.2016.04.027.

[24] Nigon GN, Burkan Isgor O, Pasebani S. The effect of annealing on the selective laser melting of 2205 duplex stainless steel: microstructure, grain orientation, and manufacturing challenges. Opt Laser Technol 2021;134:106643. https://doi.org/10.1016/j.optlastec.2020.106643.

[25] Hosseini VA, Högström M, Hurtig K, Valiente Bermejo MA, Stridh LE, Karlsson L. Wire-arc additive manufacturing of a duplex stainless steel: thermal cycle analysis and microstructure characterization. Weld World 2019;63:975–87. https://doi.org/10.1007/s40194-019-00735-y.

[26] Zhang X, Wang K, Zhou Q, Kong J, Peng Y, Ding J, et al. Element partitioning and electron backscatter diffraction analysis from feeding wire to as-deposited microstructure of wire and arc additive manufacturing with super duplex stainless steel. Mater Sci Eng, A 2020;773:138856. https://doi.org/10.1016/j.msea.2019.138856.

[27] Posch G, Chladil K, Chladil H. Material properties of CMT—metal additive manufactured duplex stainless steel blade-like geometries. Weld World 2017;61:873–82. https://doi.org/10.1007/s40194-017-0474-5.

[28] Lervåg M, Sørensen C, Robertstad A, Brønstad BM, Nyhus B, Eriksson M, et al. Additive manufacturing with superduplex stainless steel wire by cmt process. Metals 2020;10:5–12. https://doi.org/10.3390/met10020272.

[29] Stuzer J, Totzauer T, Wittig B, Zinke M, Juttner S. GMAW cold wire technology for adjusting the manufactured duplex stainless steel components. Metals 2019;9:564–83. https://doi.org/10.3390/met9050564.

[30] Zhang X, Wang K, Zhou Q, Ding J, Ganguly S, Grasso M, et al. Microstructure and mechanical properties of TOP-TIG-wire and arc additive manufactured super duplex stainless steel (ER2594). Mater Sci Eng, A 2019;762:138097. https://doi.org/10.1016/j.msea.2019.138097.

[31] Zhang Y, Cheng F, Wu S. The microstructure and mechanical properties of duplex stainless steel components fabricated via flux-cored wire arc-additive manufacturing. J Manuf Process 2021;69:204–14. https://doi.org/10.1016/j.jmapro.2021.07.045.

[32] Wanwan J, Chaoqun Z, Shuoya J, Yingtao T, Daniel W, Wen L. Wire Arc additive manufacturing of stainless steels: a review. Appl Sci 2020;10:1563. https://doi.org/10.3390/app10051563.

[33] Hejripour F, Binesh F, Hebel M, Aidun DK. Thermal modeling and characterization of wire arc additive manufactured duplex stainless steel. J Mater Process Technol 2019;272:58–71. https://doi.org/10.1016/j.jmatprotec.2019.05.003.

[34] Eriksson M, Lervåg M, Sørensen C, Robertstad A, Brønstad BM, Nyhus B, et al. Additive manufacture of superduplex stainless steel using WAAM. MATEC Web Conf 2018;188:1–8. https://doi.org/10.1051/matecconf/201818803014.

[35] Baghdadchi A, Hosseini VA, Valiente Bermejo MA, Axelsson B, Harati E, Högström M, et al. Wire laser metal deposition additive manufacturing of duplex stainless steel components — development of a systematic methodology. Materials 2021;14:7170. https://doi.org/10.3390/ma14237170.

[36] Jiang D, Birbilis N, Hutchinson CR, Brameld M. On the microstructure and electrochemical properties of additively manufactured duplex stainless steels produced using laser-powder bed fusion. Corrosion 2020;76:871–83. https://doi.org/10.5006/3571.

[37] Haghdadi N, Laleh M, Chen H, Chen Z, Ledermueller C, Liao X, et al. On the pitting corrosion of 2205 duplex stainless steel produced by laser powder bed fusion additive manufacturing in the as-built and post-processed conditions. Mater Des 2021;212:110260. https://doi.org/10.1016/j.matdes.2021.110260.

[38] Kotecki DJ. Heat treatment of duplex stainless steel weld metals. Weld J 1989;68:431s–41s.

[39] Schneider CA, Rasband WS, Eliceiri KW. NIH Image to ImageJ: 25 years of image analysis. Nat Methods 2012;9:671–5. https://doi.org/10.1038/nmeth.2089.

[40] ASTM G. 61-86 standard test method for conducting cyclic potentiodynamic polarization measurements for localized corrosion susceptibility of iron. ASTM Stand 2001;3:223–7.

[41] ASTM G150-18 standard test method for electrochemical critical pitting temperature testing of stainless steels and related alloys. ASTM Int; 2018.

[42] Alvarez-Armas I, Degallaix-Moreuil S. Duplex stainless steels. John Wiley & Sons; 2013.

[43] Wang L, Felicelli S, Gooroochurn Y, Wang PT, Horstemeyer MF. Optimization of the LENS® process for steady molten pool size. Mater Sci Eng, A 2008;474:148–56. https://doi.org/10.1016/j.msea.2007.04.119.

[44] Akbari M, Kovacevic R. An investigation on mechanical and microstructural properties of 316LSi parts fabricated by a robotized laser/wire direct metal deposition system. Addit Manuf 2018;23:487–97. https://doi.org/10.1016/j.addma.2018.08.031.

[45] Shamsaei N, Yadollahi A, Bian L, Thompson SM. An overview of Direct Laser Deposition for additive manufacturing; Part II: mechanical behavior, process parameter optimization and

control. Addit Manuf 2015;8:12–35. https://doi.org/10.1016/j.addma.2015.07.002.

[46] Xu X, Mi G, Luo Y, Jiang P, Shao X, Wang C. Morphologies, microstructures, and mechanical properties of samples produced using laser metal deposition with 316 L stainless steel wire. Opt Laser Eng 2017;94:1–11. https://doi.org/10.1016/j.optlaseng.2017.02.008.

[47] Yang Y, Wang Z, Tan H, Hong J, Jiang Y, Jiang L, et al. Effect of a brief post-weld heat treatment on the microstructure evolution and pitting corrosion of laser beam welded UNS S31803 duplex stainless steel. Corrosion Sci 2012;65:472–80. https://doi.org/10.1016/j.corsci.2012.08.054.

[48] Bettini E, Kivisäkk U, Leygraf C, Pan J. Study of corrosion behavior of a 22% Cr duplex stainless steel: influence of nano-sized chromium nitrides and exposure temperature. Electrochim Acta 2013;113:280–9. https://doi.org/10.1016/j.electacta.2013.09.056.

[49] Kang DH, Lee HW. Study of the correlation between pitting corrosion and the component ratio of the dual phase in duplex stainless steel welds. Corrosion Sci 2013;74:396–407. https://doi.org/10.1016/j.corsci.2013.04.033.

[50] Yang Y, Yan B, Li J, Wang J. The effect of large heat input on the microstructure and corrosion behaviour of simulated heat affected zone in 2205 duplex stainless steel. Corrosion Sci 2011;53:3756–63. https://doi.org/10.1016/j.corsci.2011.07.022.

[51] Srinivasan J, Kelly RG. One-dimensional pit experiments and modeling to determine critical factors for pit stability and repassivation. J Electrochem Soc 2016;163:C759.

[52] Dunn DS, Cragnolino GA, Sridhar N. An electrochemical approach to predicting long-term localized corrosion of corrosion-resistant high-level waste container materials. Corrosion 2000;56:90–104. https://doi.org/10.5006/1.3280526.

[53] G192-08 A. Standard test method for determining the crevice repassivation potential of corrosion-resistant alloys using a potentiodynamic-Galvanostatic-potentiostatic technique 2008.